Supporting Information:

Ultrafast Charge Relocation Dynamics in Enol - Keto Tautomerization Monitored with a Local Soft-X-ray Probe

Micheline B. Soley,[†,‡,‖] Pablo E. Videla,[†,¶,‖] Erik T. J. Nibbering,[§] and Victor S. Batista[∗,†,¶,‡]

†Department of Chemistry, Yale University, P.O. Box 208107, New Haven, CT, 06520-8107, USA

‡Yale Quantum Institute, Yale University, P.O. Box 208334, New Haven, CT, 06520-8263, USA

¶Energy Sciences Institute, Yale University, P.O. Box 27394, West Haven, CT, 06516-7394, USA

§Max Born Institute for Nonlinear Optics and Short Pulse Spectroscopy, Max Born Strasse 2A, 12489 Berlin, Germany

‖Contributed equally to this work

E-mail: victor.batista@yale.edu

Methods

In order to provide a highly accurate probe of the HBT isomerization mechanism, we simulate the UV-pump/soft X-ray probe spectroscopy with quantum treatment of all degrees of freedom as follows: The *ab initio* ground and excited-state potential energy surfaces are generated at the TDDFT level of theory, and the ground-state wavefunction is identified according to imaginary time propagation in the ground electronic state and instantaneously shifted to the excited electronic state to model the UV pump, with quantum dynamics of the molecule computed according to the low-rank tensor train split-operator Fourier transform (TT-SOFT) method. The resulting time-resolved X-ray spectra are computed as a convolution of the wavepacket with K-edge core excitations with transition energies and dipole strengths determined with the Maximum Overlap Method (MOM) and Time-Dependent DFT (TDDFT).

Potential Energy Surface

We describe the dynamics of HBT following photoexcitation in terms of full-dimensional ground and excited-state potentials based on a reaction surface approach[1–3], similar to the ones implemented in earlier studies of ESIPT.[4–6] In the present work, we use mass-weighted normal modes, determined at the transition state of the S_1 electronic state, as generalized coordinates to characterize the proton transfer dynamics. The normal mode displacement associated with the imaginary frequency is selected as the proton transfer reactive coordinate Q_1. Additionally, the normal mode with predominantly components along the CCC internal in-plane bending mode Q_2 is included. The latter modulates the N$-$O distance between the proton donor and acceptor moieties and is expected to be strongly coupled to Q_1. Figure 2 shows the normal mode displacements.

Each full-dimensional potential energy surface $V(Q_1, Q_2, \mathbf{z})$ is constructed as a quadratic

expansion around a two-dimensional reaction surface potential $V_0(Q_1, Q_2)$,

$$V(Q_1, Q_2, \mathbf{z}) = V_0(Q_1, Q_2) + \frac{1}{2}[\mathbf{z} - \mathbf{z_0}(Q_1, Q_2)] \cdot \mathbf{K}(Q_1, Q_2) \cdot [\mathbf{z} - \mathbf{z_0}(Q_1, Q_2)], \qquad (1)$$

where $\mathbf{z}$ represents the other 67 vibrational normal modes that are described as locally harmonic oscillators with force constants $\mathbf{K}(Q_1, Q_2)$ and equilibrium positions $\mathbf{z_0}(Q_1, Q_2)$ parametrized by the reaction coordinates $Q_{1,2}$. The *ab initio* ground and excited-state surfaces $V_0(Q_1, Q_2)$ are determined by fully optimizing the geometry of the system with respect to all other degrees of freedom $\mathbf{z}$, subject to the constraint of a fixed value of $Q_{1,2}$, at 12 and 20 equally spaced points in the range $Q_1 \in [-50.0, 60.0]$ a.u. and $Q_2 \in [-140.0, 240.0]$ a.u., respectively. The equilibrium coordinates $\mathbf{z_0}(Q_1, Q_2)$ represent the normal mode displacements of the bath modes relative to the reference configuration and are computed by projecting the optimized $Q_{1,2}$-constrained geometry onto the normal mode displacement vectors determined at the transition state of the S_1 electronic state. The force constants $\mathbf{K}(Q_1, Q_2)$ representing the bath couplings are determined by computing the (mass-weighted) Hessian at each optimized $Q_{1,2}$-constrained geometry and projecting out the contribution due to the $Q_{1,2}$ reactive coordinates.[2]

A hierarchical set of approximations can be applied to Eq. (1). If one neglects the coupling between the different bath modes (i.e. neglecting non-diagonal elements in $\mathbf{K}(Q_1, Q_2)$), the potential reduces to

$$V(Q_1, Q_2, \mathbf{z}) = V_0(Q_1, Q_2) + \sum_j \frac{1}{2} K_{jj}(Q_1, Q_2)[z_j - z_{j,0}(Q_1, Q_2)]^2. \qquad (2)$$

If one further neglects the dependence of $\mathbf{K}(Q_1, Q_2)$ on $Q_{1,2}$, the potential reduces to

$$V(Q_1, Q_2, \mathbf{z}) = V_0(Q_1, Q_2) + \sum_j \frac{1}{2}\omega_j^2[z_j - z_{j,0}(Q_1, Q_2)]^2 \qquad (3)$$

with $\omega_j^2 = K_{jj}(Q_1 = 0, Q_2 = 0)$. If one also neglects the $Q_{1,2}$-dependence on $\mathbf{z_0}(Q_1, Q_2)$, the

potential reduces to

$$V(Q_1, Q_2, \mathbf{z}) = V_0(Q_1, Q_2) + \sum_j \frac{1}{2}\omega_j^2 z_j^2 \tag{4}$$

where we have used the fact that $z_{j,0}(Q_1 = 0, Q_2 = 0) = 0$.

All excited-state calculations were performed at the TDDFT level of theory using the ωB97XD functional[7] and cc-pvdz basis set,[8] as implemented in Gaussian 16.[9] Solvent effects (dichloromethane) were included implicitly through the PCM polarizable continuum model.[10–14]

To test the accuracy of the potential energy surface, in Figure 1 we present the (harmonic) IR spectra in the C=O spectral region for HBT in the S_0-enol and S_1-keto conformations. The ground-state spectrum is characterized by signals corresponding to C-C stretching and C-H rocking modes, and is in reasonable agreement with the experimental steady-state IR of HBT in non-polar solvents.[5,6] After photoexcitation and enol-to-keto transformation, a new feature appears at 1544 cm^{-1}, corresponding to the C=O stretching mode of the keto conformer, in excellent agreement with UV-pump IR-probe experimental observations.[5,6]

These coarsely grained TDDFT potentials are used to generate a finer position-space grid to improve the accuracy of the quantum dynamics simulation in the reactive potential $V(Q_1, Q_2)$. Potential values at positions intermediate between grid points are determined according to cubic splines, and potential values at positions outside of the original position space domain are defined to be equal to the value at the edge of the original domain. The resulting reactive potential energy surface is shown in Fig. 2 with representative large-amplitude mode dependent displacements and coupling constants in Fig. 3.

To reduce the computational cost associated with evaluation of the potential at all points on the 69-dimensional position space grid, the potential is compressed according to the low-
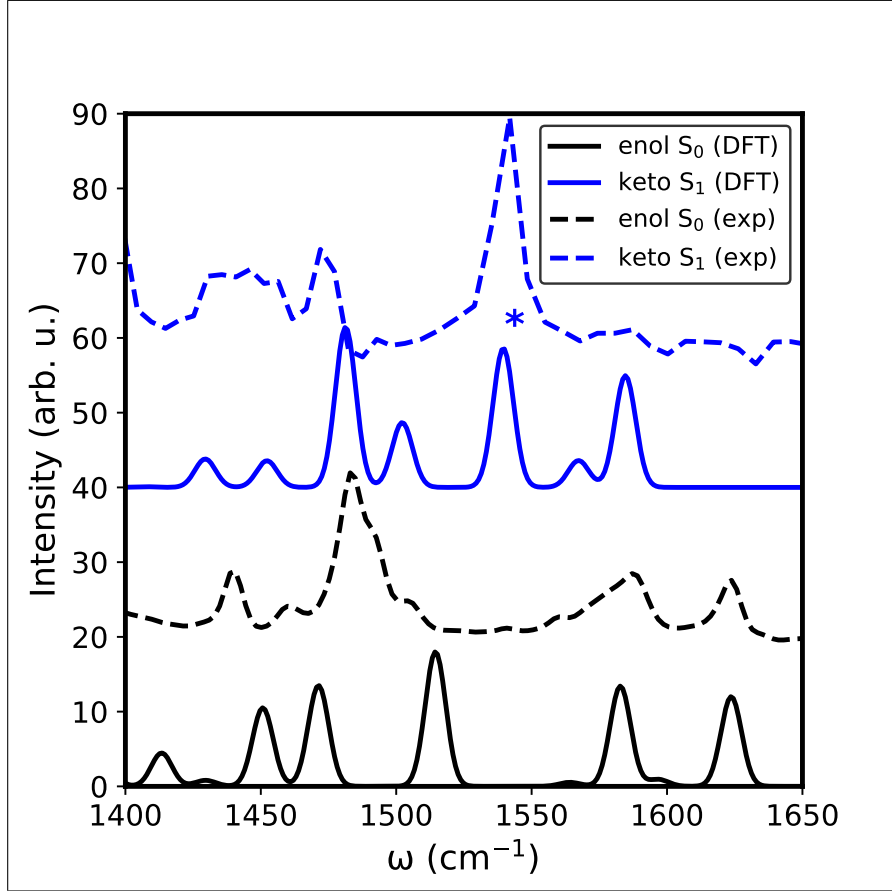
Figure 1: IR spectra (scaled by 0.95) for HBT in the enol S_0 state (black lines) and keto S_1 state (blue lines). Experimental spectra were obtained from Refs.[5,6]. The band corresponding to the C=O stretching mode in the S_1-keto conformation is marked by the asterisk.
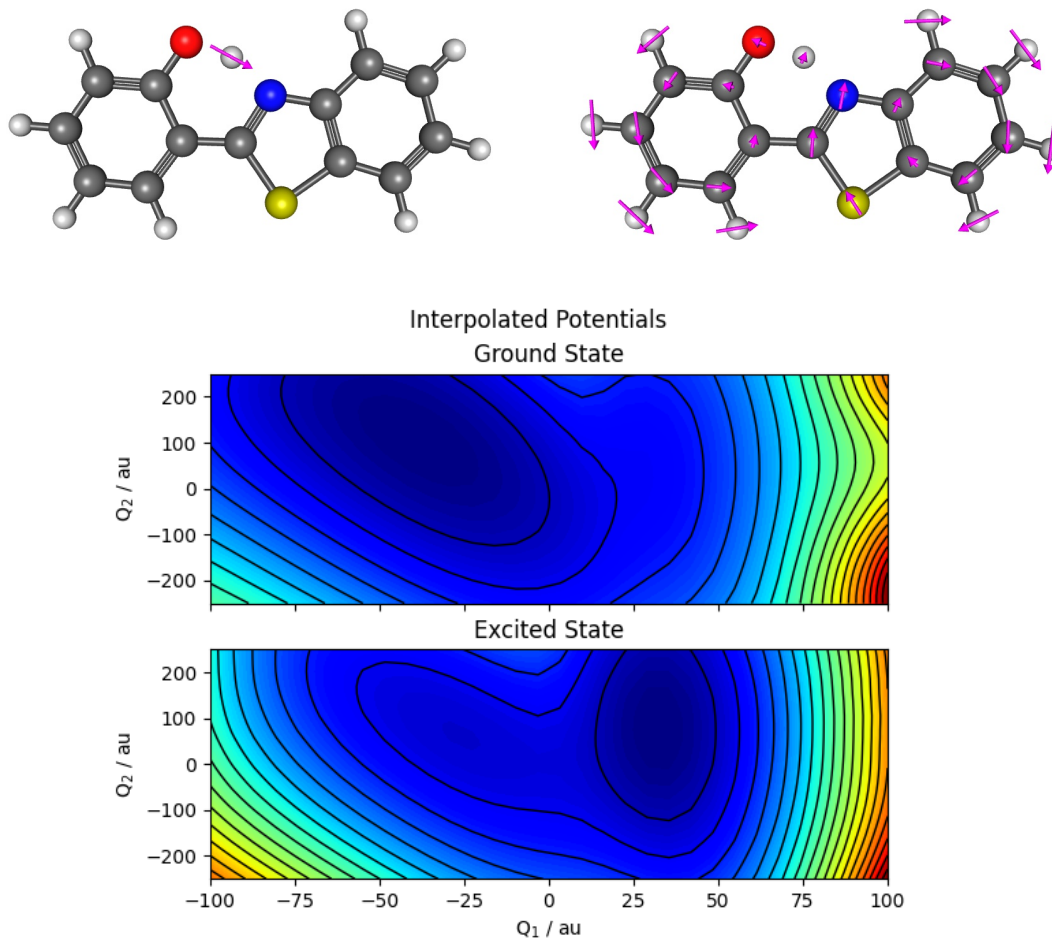
Figure 2: Top: Normal mode displacements of the large-amplitude modes associated with the proton transfer coordinate Q_1 and CCC internal in-plane bending coordinate Q_2. Bottom: Reactive potential energy surfaces $V_0(Q_1, Q_2)$ of the S_0 and S_1 electronic states as a function of the large-amplitude modes Q_1 and Q_2.
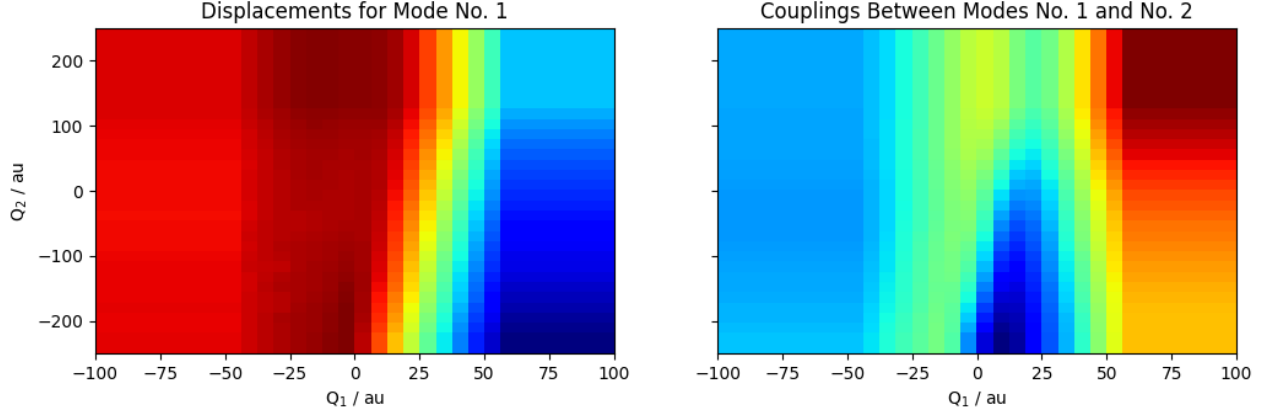
Figure 3: Representative *ab initio* Q_1 and Q_2 large-amplitude mode dependent displacement (left) and coupling constant (right). In the adiabatic approximation, coupling constants are fixed to their $(Q_1, Q_2) = (0, 0)$ a.u. value.

rank tensor-train approximation,[15,16] a form of matrix product states[17] defined as follows:

$$Q(i_1, ..., i_d) \approx \sum_{\alpha_1=1}^{r_1} \sum_{\alpha_2=1}^{r_2} \ldots \sum_{\alpha_{d-1}=1}^{r_{d-1}} A_1(1, i_1, \alpha_1) A_2(\alpha_1, i_2, \alpha_2) \ldots A_d(\alpha_{d-1}, i_d, 1), \qquad (5)$$

where i_j corresponds to the position space coordinates in physical dimension j and A_j is a three-mode tensor contracted to the neighboring tensors by indices α_{j-1} and α_j. The low-rank tensor-train decomposition is adaptively computed via the cross approximation.[15]

Dynamics

To monitor atomic motion in the HBT isomerization process, the *ab initio* potential energy surfaces are used to simulate dynamics of the HBT molecule with tensor-train split-operator Fourier transform (TT-SOFT) quantum dynamics. This method is employed to accurately incorporate quantum effects on the isomerization process, as it treats all of the molecule's 69 normal modes fully quantum mechanically.[18] Tensor train manipulations are performed with Oseledet's TT-Toolbox for fast interpolation procedure[19] via the cross approximation,[15] which avoids calculation of the potential and wavepackets at all points on the position space grid. Tensor trains are evaluated with an relative accuracy parameter of $\epsilon = 10^{-14}$ and a maximum rank of $r_{\max} = 10$ to yield an accurate, low-cost representation of physical

quantities such as the potential energy surface, wavepacket, and propagators.

TT-SOFT is employed for imaginary time propagation in the ground electronic state potential energy surface S_0 to determine the initial ground-state wavepacket. The ground-state wavepacket is then instantaneously excited to the excited electronic state S_1, whereupon real time propagation is used to investigate excited-state intramolecular proton transfer (ESIPT).

Both imaginary and real time propagation are carried out for $N_\tau = 800$ time steps of length $\tau = 12.5$ a.u. to accurately follow the motion of short wavelength normal modes, ensure convergence of the ground-state wavefunction, and follow the isomerization process, which is known experimentally to occur within $T = 250$ fs.[4,5,20,21] The position space grid in each direction is discretized into $N_p = 2^5$ equally spaced gridpoints for sufficient resolution of the potential energy surface. The large-amplitude modes are considered in the domain $Q_1 \in \{-100, 100\}$ a.u. and $Q_2 \in \{-250, 250\}$ a.u. and the bath modes are considered in the domain $Q_i \in \{-\frac{10}{\sqrt{\omega_i}}, \frac{10}{\sqrt{\omega_i}}\}$ to include the full extent of the wavepacket motion. Prior to imaginary time propagation, the wavepacket is initialized as a Gaussian wavefunction with a noise factor

$$\psi_0(\mathbf{x}) = \prod_{j=1}^{D} \sqrt[4]{\frac{m\omega_j}{\pi}} e^{\frac{m\omega_j}{2\sigma_j^2}(x_j - x_0)^2} + 10^{-16}\Theta(j - 50) \tag{6}$$

$$\Theta(j) = \begin{cases} 1 & j \geq 0 \\ 0 & j < 0 \end{cases} \tag{7}$$

for particle mass $m = 1$ and frequency ω_j, width parameter σ_j, and center x_j of normal mode j for D dimensions. To initialize the wavepacket close to the true ground-state wavefunction while encouraging sampling of nonzero points in the cross approximation interpolation procedure, the Gaussian is initially centered at a position slightly shifted from the minimal position of the ground-state potential energy surface to facilitate fast identification of the ground-state wavefunction ($x_0 = -32.5$ a.u., $x_1 = 123.515625$ a.u., $x_i = z_{i,0}(0,0)$ for $i > 2$).

The Gaussian widths of the large-amplitude modes are defined by the harmonic approximation for the ground-state well ($\sigma_1 = 22.473$ a.u. and $\sigma_2 = 53.132$ a.u.) and those of the bath modes are defined in terms of the couplings ($\sigma_i = \sqrt{\frac{2}{\omega_i}}$ for $i > 2$).

The HBT motion represented by propagation of the initial wavepacket is evaluated by computing the average expectation value of position of each coordinate, which is given by the inner product of the wavefunction and the corresponding position-space operator acting on the wavefunction.

Time-Resolved UV-Pump/X-Ray Probe Spectra

The overall behavior of the HBT molecule during isomerization is investigated via prediction of the transient X-ray absorption spectrum (TRAXS). The transient X-ray spectral lineshape is modeled as an incoherent superposition of core excitations weighted by the magnitude of the nuclear wavepacket at a given time instant, namely

$$I(\omega, t) = \sum_k \int d\mathbf{Q} \; |\Psi(\mathbf{Q}, t)|^2 |\mu_k(\mathbf{Q})|^2 \delta(\omega - \omega_k(\mathbf{Q})) \tag{8}$$

where $\Psi(\mathbf{Q}, t)$ represents the wavepacket at time t and nuclear coordinates $\mathbf{Q}$, ω is the photon energy, and $\omega_k(\mathbf{Q})$ and $\mu_k(\mathbf{Q})$ correspond to the k-th electronic transition energy and transition strength, respectively.

In the present work, for simplicity we approximate the nuclear density along the bath modes by a Dirac delta function at the expectation value of the position operator, given by $\bar{\mathbf{z}} = \int d\mathbf{Q} \; |\Psi(\mathbf{Q}, t)|^2 \mathbf{z}$. Therefore, the transient X-ray spectrum was calculated as

$$I(\omega, t) = \sum_k \int dQ_1 dQ_2 \; |\Psi(Q_1, Q_2, \bar{\mathbf{z}}, t)|^2 |\mu_k(Q_1, Q_2, \bar{\mathbf{z}})|^2 \delta(\omega - \omega_k(Q_1, Q_2, \bar{\mathbf{z}})) \tag{9}$$

The evaluation of the integral over the $Q_{1,2}$ quantum coordinates was performed by Monte Carlo sampling, using the ratio between the nuclear density as the acceptance parameter in the Metropolis algorithm.[22] Forty configurations were sufficient to converge the spectra. The

spectral sticks were broadened with a Lorentzian envelope with full width at half maximum of 0.5 eV to approximate the core-hole lifetime broadening of each atom and take into account experimental resolution.

The X-ray transition energies and dipole strengths for the excited S_1 state were obtained by a combined Maximum Overlap Method (MOM)[23,24] and Time-Dependent DFT[25] approach as implemented in the Q-Chem package.[26] The MOM strategy was used to obtained the S_1 electronic wavefunction, which was subsequently used as a reference state to perform TDDFT core excitations. The initial guess for the MOM-SCF procedure was taken as $[\text{HOMO}(\alpha)]^1[\text{LUMO}(\beta)]^1$ to resemble the hole and particle NTO of the transition from the ground state to the valence-excited state. We used the initial MOM (IMOM) method[23,24] instead of standard MOM to ensure convergence to the desired S_1 reference electronic state. From the S_1 reference state, TDDFT calculations were performed with a reduced single-excitation space that included the nitrogen or oxygen 1s orbital and all the virtual orbitals to obtain 30 core-valence X-ray excitations. All calculations were performed using the ωB97XD functional[7] and cc-pvdz basis set,[8] with dichloromethane employed as implicit solvent through PCM.[10–14]

Fully Quantum Treatment of 69D Dynamics

The fully quantum treatment of HBT dynamics successfully reproduced known behaviors of the HBT isomerization reaction. The average trajectory was found to be in agreement with previous experimental and theoretical findings, as shown in Fig. 4. The expectation value of the OH normal mode coordinate Q_1 shifted from a position in the enol* well to the keto* well within 200 fs, in agreement with previous results that suggest excited-state intramolecular proton transfer (ESIPT) occurs within 200 fs.[4,5,20,21] The expectation value of the OH stretch coordinate remained in the keto* well for the remainder of the examined dynamics, which agrees with previous findings that suggest equilibrium is achieved within 400 to 600 fs. The expectation value of the large-amplitude mode coordinate corresponding

to the CCC normal mode exhibited an oscillation with a period on the order of 250 fs, which suggests proton/hydrogen transfer is accompanied by a ring-bending motion on the same timescale. The theoretically determined population of keto isomers supported previous findings that significant keto* formation occurs within the first 50 fs of dynamics and features oscillations on timescales below 50 fs.[4]
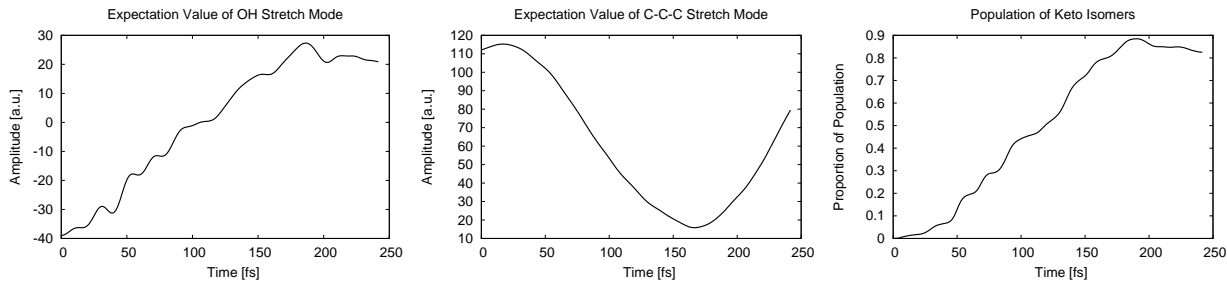

Figure 4: Expectation value of position of the large amplitude mode coordinates Q_1 (left) and Q_2 (center) and population of the keto isomer (right) confirmed the expected dynamics of HBT isomerization.

Further support for the accuracy of the quantum simulation was given by the probability density evaluated at the large amplitude mode coordinates (holding bath mode positions fixed at their expectation value, see Fig. 5). The tunneling of the wavepacket out of the enol* well in the first 50 fs and into the keto* well within the first 250 fs was in agreement with previous experimental and theoretical results, as was the equilibration of the wavepacket in the enol* well for the remainder of the simulated dynamics.

Furthermore, the probability density demonstrated tunneling plays a significant role in the isomerization process. At 90 fs − 240 fs after the instantaneous pump, both the keto* and enol* isomer states are observed, in line with the hypothesis that HBT isomerization does not occur in a concerted fashion and involves quantum effects in which both isomers participate in the isomerization process. The dynamics therefore reflected the full range of behaviors involved in HBT isomerization, including OH and CCC normal mode oscillations and tunneling effects.
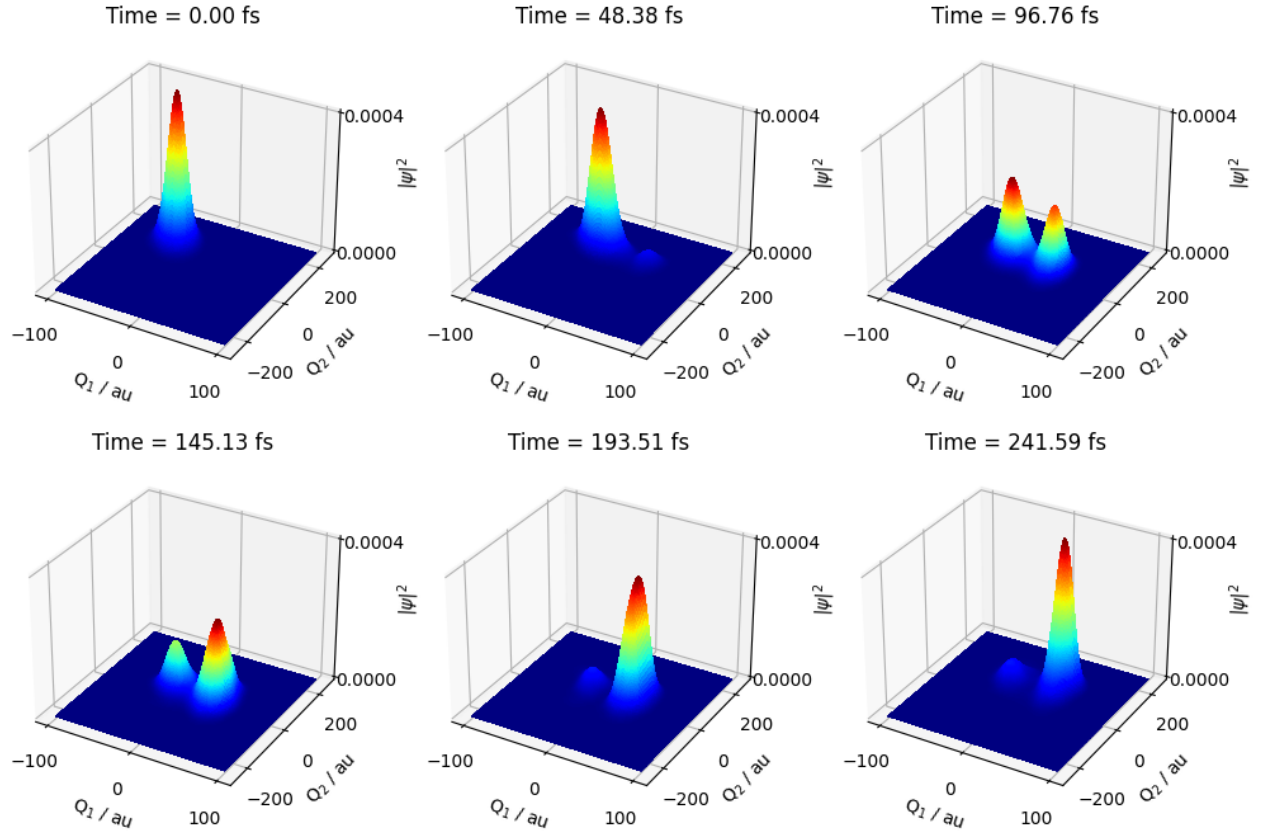
11

Figure 5: Probability density in terms of large amplitude mode coordinates Q_1 and Q_2 during the HBT isomerization process with integration over quantum bath modes.

Evaluation of Potential and Spectrum Approximations

The accuracy of the 69-dimensional potential energy surface was evaluated through comparisons of dynamics and transient absorption X-ray spectra for varying rank, numbers of quantum bath modes, approximations to the full potential energy surface, and trajectory sampling.

The accuracy of the low-rank approximation to the reactive potential is verified in Fig. 6. Cross approximation of the reactive potential without subsequent rounding to a lower rank yields a reactive potential in agreement with the rank four result, which suggests the maximal rank 10 used to generate the dynamics is sufficient to accurately reproduce the potential energy surface. Similar results are obtained for the coupling and displacement parameters, as shown for the examples in Fig. 7.
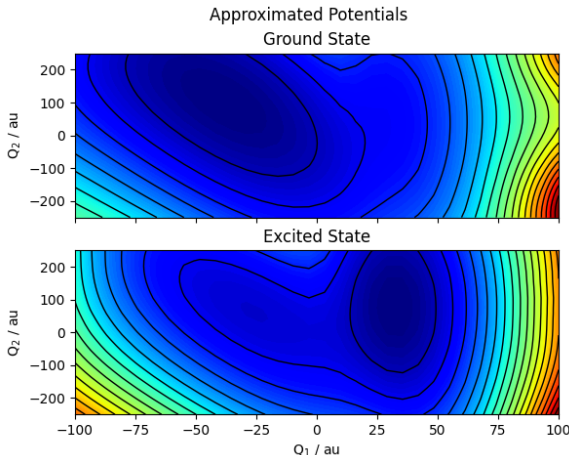

Figure 6: Low-rank tensor-train approximation of reactive potential.

Evaluation of the dynamics for differing numbers of quantum bath modes supports the need for inclusion of a large number of bath modes for successful simulation of HBT isomerization. As shown in Fig. 8, inclusion of only the reactive coordinates is insufficient to model irreversible formation of the keto isomer, as the molecular system is unable to dissipate energy into the bath coordinates. This results in periodic reformation of the enol isomer. As the number of bath modes included is increased, HBT approaches aperiodic formation of the
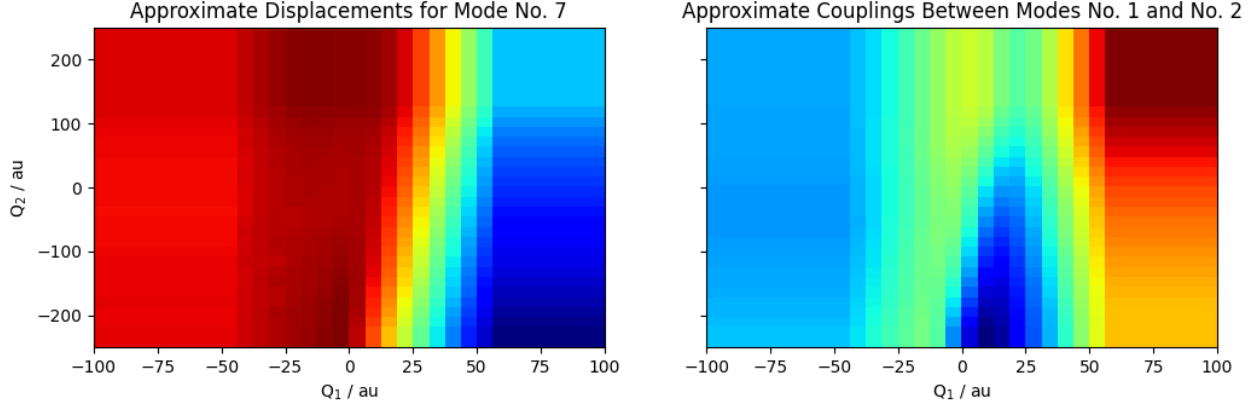
Figure 7: Low-rank tensor-train approximation of an example large-amplitude mode dependent (left) displacement and (right) coupling constant.
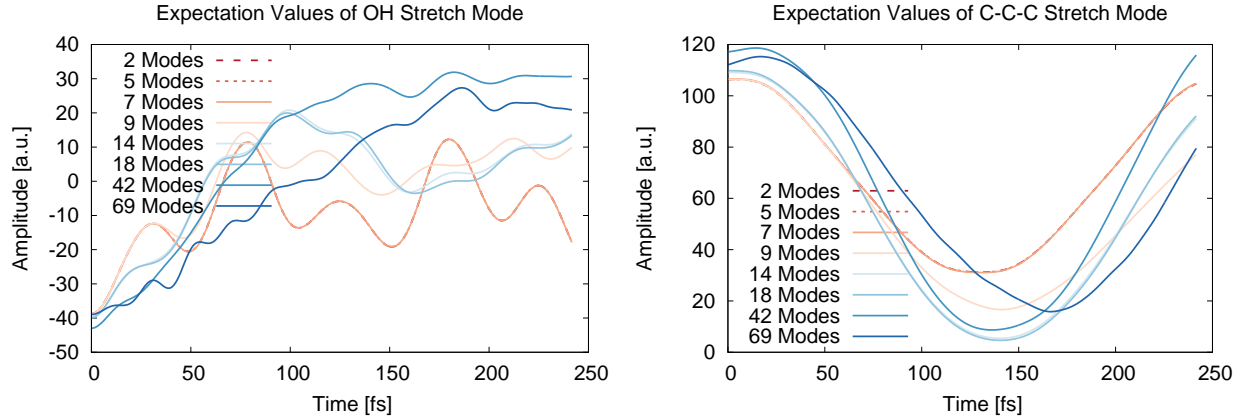
keto isomer as expected from previous UV-IR experiments.

Figure 8: Expectation value of the large-amplitude mode coordinates Q_1 and Q_2 with inclusion of zero to 67 bath modes.

The need to include a large number of bath modes to simulate equilibration of the keto isomer is also supported by visualization of the probability density as a function of the number of large-amplitude modes, as shown in Figs. 5 and 9. In lower-dimensional examples, the wavepacket tunnels back and forth between the two isomeric wells, whereas the 69D result yields the expected irreversible keto formation.

In Figure 10, we present the time-resolved (TR) N and O K-edge XANES of HBT after photoexcitation for the 2D model, without bath modes. The TR spectra is characterized by well-separated peaks near 384 eV and 388 eV in the N K-edge spectrum and 516 eV, 520 eV,
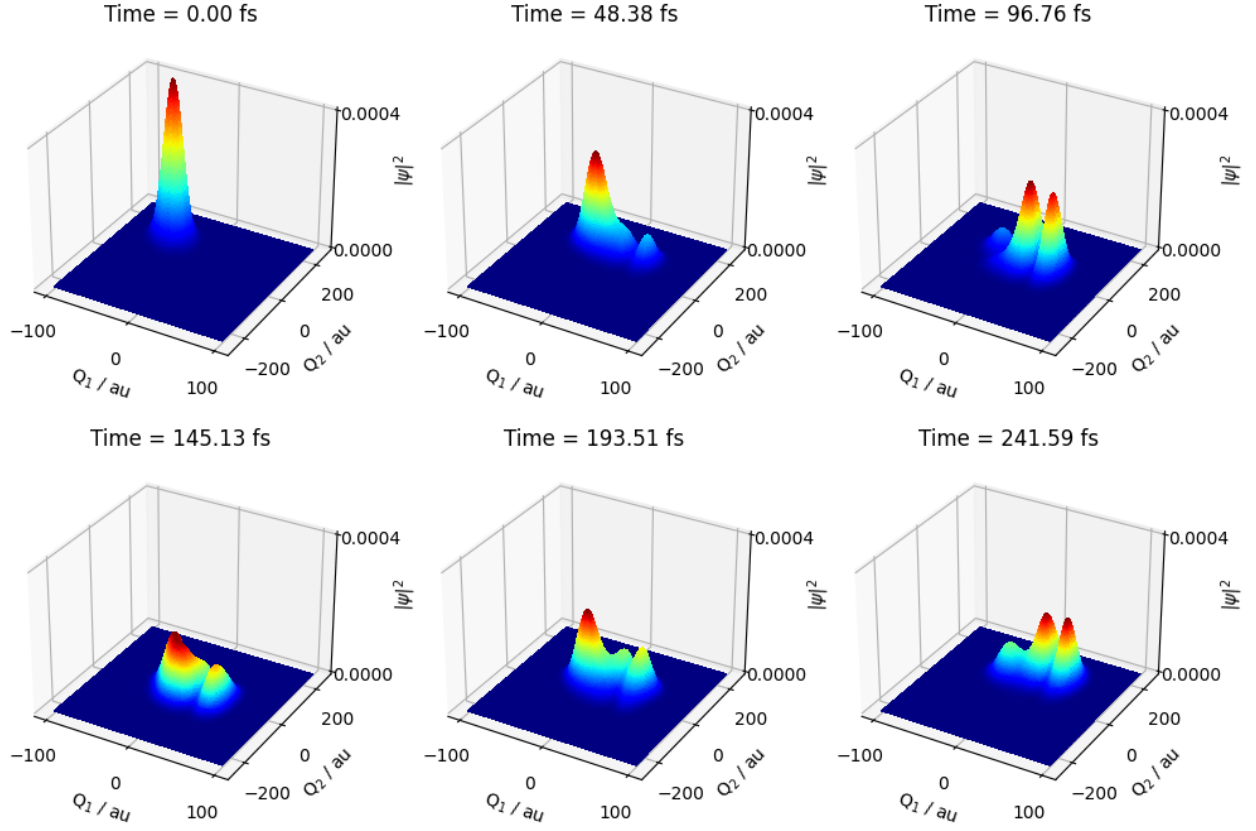
Time = 0.00 fs

Time = 48.38 fs

Time = 96.76 fs

Time = 145.13 fs

Time = 193.51 fs

Time = 241.59 fs

Figure 9: Probability density as a function of the large-amplitude mode coordinates Q_1 and Q_2 with integration over the 18 lowest frequency bath modes.

and 522 eV in the O K-edge spectrum. In the absence of the quantum bath modes, the peak oscillations closely agree with the oscillations of the expectation values of the large-amplitude mode coordinates on which the spectra are based. As in the expectation value of position of the coordinates, the spectral peaks at the initial and final times examined agree, which suggests a reformation of reactants indicative of the absence of the needed quantum bath.
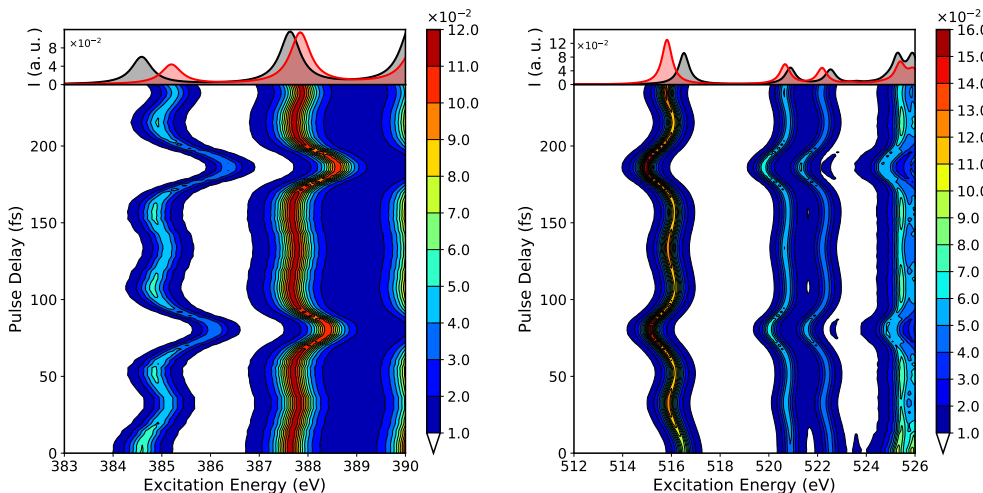

Figure 10: N K-edge (left) and O K-edge (right) TRXAS for HBT after photoexcitation with consideration of only the large-amplitude modes and omitting bath modes. Inset panel shows NEXAFS spectra at the initial enol* (black curve) and final keto* (red curve) conformation.

Fig. 11 illustrates the improved accuracy of the TRXAS spectra from Monte Carlo sampling of the probability density in contrast to inclusion only of the average trajectory. Whereas the TRXAS computed via Monte Carlo sampling includes paired peaks at the reactant and product frequencies during the isomerization process in the O and N K-edge spectra, the TRXAS computed only with average trajectories yields a single peak that interpolates between these two values. This suggests sampling of the probability density beyond the average trajectory is required to demonstrate the full role of quantum effects in the isomerization process. Nonetheless, the average trajectory is valuable in isolating the reactant and product frequencies in the TRXAS as well as the overall time-dependent behavior of the molecule.
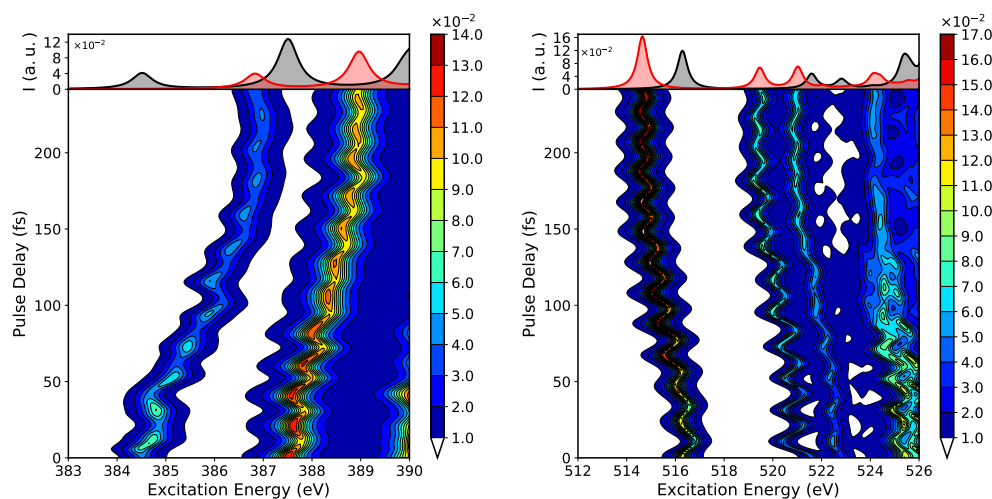
Figure 11: N K-edge (left) and O K-edge (right) TRXAS for HBT after photoexcitation considering the average trajectory. Inset panel shows NEXAFS spectra at the initial enol* (black curve) and final keto* (red curve) conformation.
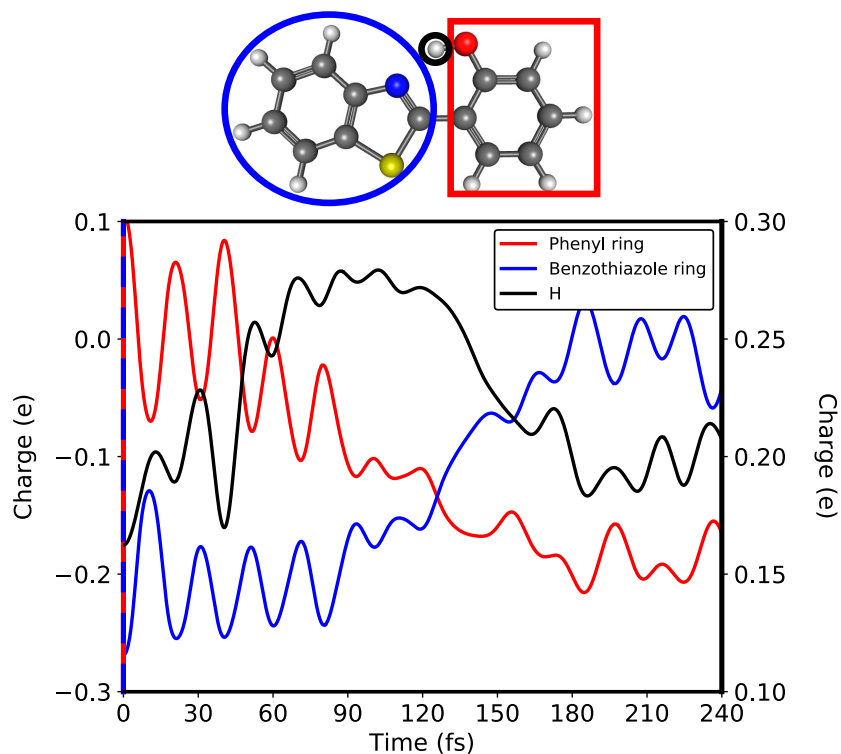
Charge Dynamics

Figure 12: Time evolution of the Mulliken charges on the phenyl ring, benzothiazole ring and and transferring H atom. Note the different scale of the data (as indicated by the colored border of the axis).

References

(1) Miller, W. H.; Handy, N. C.; Adams, J. E. Reaction Path Hamiltonian for Polyatomic Molecules. *J. Chem. Phys.* **1980**, *72*, 99–112.

(2) Carrington, T.; Miller, W. H. Reaction Surface Hamiltonian for the Dynamics of Reactions in Polyatomic Systems. *J. Chem. Phys.* **1984**, *81*, 3942–3950.

(3) Carrington, T.; Miller, W. H. Reaction Surface Description of Intramolecular Hydrogen Atom Transfer in Malonaldehyde. *J. Chem. Phys.* **1986**, *84*, 4364–4370.

(4) Kim, J.; Wu, Y.; Brédas, J.-L.; Batista, V. S. Quantum Dynamics of the Excited-State Intramolecular Proton Transfer in 2-(2'-Hydroxyphenyl)benzothiazole. *Isr. J. Chem.* **2009**, *49*, 187–197.

(5) Luber, S.; Adamczyk, K.; Nibbering, E. T. J.; Batista, V. S. Photoinduced Proton Coupled Electron Transfer in 2-(2'-Hydroxyphenyl)-Benzothiazole. *J. Phys. Chem. A* **2013**, *117*, 5269–5279.

(6) Mohammed, O. F.; Luber, S.; Batista, V. S.; Nibbering, E. T. J. Ultrafast Branching of Reaction Pathways in 2-(2'-Hydroxyphenyl)benzothiazole in Polar Acetonitrile Solution. *J. Phys. Chem. A* **2011**, *115*, 7550–7558.

(7) Chai, J.-D.; Head-Gordon, M. Long-Range Corrected Hybrid Density Functionals With Damped Atom–Atom Dispersion Corrections. *Phys. Chem. Chem. Phys.* **2008**, *10*, 6615–6620.

(8) Dunning, T. H. Gaussian Basis Sets for Use in Correlated Molecular Calculations. I. The Atoms Boron Through Neon and Hydrogen. *J. Chem. Phys.* **1989**, *90*, 1007–1023.

(9) Frisch, M. J. et al. Gaussian 16 Revision C.01. 2016; Gaussian Inc. Wallingford CT.

(10) Cancès, E.; Mennucci, B.; Tomasi, J. A New Integral Equation Formalism for the Polarizable Continuum Model: Theoretical Background and Applications to Isotropic and Anisotropic Dielectrics. *J. Chem. Phys.* **1997**, *107*, 3032–3041.

(11) Mennucci, B.; Cancès, E.; Tomasi, J. Evaluation of Solvent Effects in Isotropic and Anisotropic Dielectrics and in Ionic Solutions With a Unified Integral Equation Method: Theoretical Bases, Computational Implementation, and Numerical Applications. *J. Phys. Chem. B* **1997**, *101*, 10506–10517.

(12) Tomasi, J.; Mennucci, B.; Cancès, E. The IEF Version of the PCM Solvation Method: An Overview of a New Method Addressed to Study Molecular Solutes at the QM ab Initio Level. *J. Mol. Struct.: THEOCHEM* **1999**, *464*, 211–226.

(13) Cossi, M.; Scalmani, G.; Rega, N.; Barone, V. New Developments in the Polarizable Continuum Model for Quantum Mechanical and Classical Calculations on Molecules in Solution. *J. Chem. Phys.* **2002**, *117*, 43–54.

(14) Tomasi, J.; Mennucci, B.; Cammi, R. Quantum Mechanical Continuum Solvation Models. *Chem. Rev.* **2005**, *105*, 2999–3094.

(15) Oseledets, I.; Tyrtyshnikov, E. T. TT-Cross Approximation for Multidimensional Arrays. *Linear Algebra Its Appl.* **2010**, *432*, 70–88.

(16) Oseledets, I. V. Tensor-Train Decomposition. *SIAM J. Sci. Comput.* **2011**, *33*, 2295–2317.

(17) Östlund, S.; Rommer, S. Thermodynamic Limit of Density Matrix Renormalization. *Phys. Rev. Lett.* **1995**, *75*, 3537–3540.

(18) Greene, S. M.; Batista, V. S. Tensor-Train Split-Operator Fourier Transform (TT-SOFT) Method: Multidimensional Nonadiabatic Quantum Dynamics. *J. Chem. Theory Comput.* **2017**, *13*, 4034–4042.

(19) Oseledets, I. oseledets/TT-Toolbox. 2020; https://www.github.com/oseledets/TT-Toolbox.

(20) Petrone, A.; Lingerfelt, D. B.; Williams-Young, D. B.; Li, X. Ab Initio Transient Vibrational Spectral Analysis. *J. Phys. Chem. Lett.* **2016**, *7*, 4501–4508.

(21) Chudoba, C.; Riedle, E.; Pfeiffer, M.; Elsaesser, T. Vibrational Coherence in Ultrafast Excited State Proton Transfer. *Chem. Phys. Lett.* **1996**, *263*, 622–628.

(22) Tuckermann, M. *Statistical Mechanics: Theory and Molecular Simulations*; Oxford University Press, 2010.

(23) Gilbert, A. T. B.; Besley, N. A.; Gill, P. M. W. Self-Consistent Field Calculations of Excited States Using the Maximum Overlap Method (MOM). *J. Phys. Chem. A* **2008**, *112*, 13164–13171.

(24) Barca, G. M. J.; Gilbert, A. T. B.; Gill, P. M. W. Simple Models for Difficult Electronic Excitations. *J. Chem. Theory Comput.* **2018**, *14*, 1501–1509.

(25) Dreuw, A.; Head-Gordon, M. Single-Reference ab Initio Methods for the Calculation of Excited States of Large Molecules. *Chem. Rev.* **2005**, *105*, 4009–4037.

(26) Shao, Y. Z. Gan, E. Epifanovsky, A. T. B. Gilbert, M. Wormit, J. Kussmann, A. W. Lange, A. Behn, J. Deng, X. Feng, D. Ghosh, M. Goldey P. R. Horn, L. D. Jacobson, I. Kaliman, R. Z. Khaliullin, T. Kús, A. Landau, J. Liu, E. I. Proynov, Y. M. Rhee, R. M. Richard, M. A. Rohrdanz, R. P. Steele, E. J. Sundstrom, H. L. Woodcock III, P. M. Zimmerman, D. Zuev, B. Albrecht, E. Alguire, B. Austin, G. J. O. Beran, Y. A. Bernard, E. Berquist, K. Brandhorst, K. B. Bravaya, S. T. Brown, D. Casanova, C.-M. Chang, Y. Chen, S. H. Chien, K. D. Closser, D. L. Crittenden, M. Diedenhofen, R. A. DiStasio Jr., H. Dop, A. D. Dutoi, R. G. Edgar, S. Fatehi, L. Fusti- Molnar, A. Ghysels, A. Golubeva-Zadorozhnaya, J. Gomes, M. W. D. Hanson-Heine, P. H. P.

Harbach, A. W. Hauser, E. G. Hohenstein, Z. C. Holden, T.-C. Jagau, H. Ji, B. Kaduk, K. Khistyaev, J. Kim, J. Kim, R. A. King, P. Klunzinger, D. Kosenkov, T. Kowalczyk, C. M. Krauter, K. U. Lao, A. Laurent, K. V. Lawler, S. V. Levchenko, C. Y. Lin, F. Liu, E. Livshits, R. C. Lochan, A. Luenser, P. Manohar, S. F. Manzer, S.-P. Mao, N. Mardirossian, A. V. Marenich, S. A. Maurer, N. J. Mayhall, C. M. Oana, R. Olivares-Amaya, D. P. O'Neill, J. A. Parkhill, T. M. Perrine, R. Peverati, P. A. Pieniazek, A. Prociuk, D. R. Rehn, E. Rosta, N. J. Russ, N. Sergueev, S. M. Sharada, S. Sharmaa, D. W. Small, A. Sodt, T. Stein, D. Stück, Y.-C. Su, A. J. W. Thom, T. Tsuchimochi, L. Vogt, O. Vydrov, T. Wang, M. A. Watson, J. Wenzel, A. White, C. F. Williams, V. Vanovschi, S. Yeganeh, S. R. Yost, Z.-Q. You, I. Y. Zhang, X. Zhang, Y. Zhou, B. R. Brooks, G. K. L. Chan, D. M. Chipman, C. J. Cramer, W. A. Goddard III, M. S. Gordon, W. J. Hehre, A. Klamt, H. F. Schaefer III, M. W. Schmidt, C. D. Sherrill, D. G. Truhlar, A. Warshel, X. Xua, A. Aspuru-Guzik, R. Baer, A. T. Bell, N. A. Besley, J.-D. Chai, A. Dreuw, B. D. Dunietz, T. R. Furlani, S. R. Gwaltney, C.-P. Hsu, Y. Jung, J. Kong, D. S. Lambrecht, W. Liang, C. Ochsenfeld, V. A. Rassolov, L. V. Slipchenko, J. E. Subotnik, T. Van Voorhis, J. M. Herbert, A. I. Krylov, P. M. W. Gill, and M. Head-Gordon. Advances in Molecular Quantum Chemistry Contained in the Q-Chem 4 Program Package. [Mol. Phys. 113, 184–215 (2015)].